https://doi.org/10.5194/tc-2020-245
Preprint. Discussion started: 30 October 2020

The Cryosphere Discussions
Open Access

Estimating instantaneous sea-ice dynamics from space using the bi-static radar measurements of Earth Explorer 10 candidate Harmony

Marcel Kleinherenbrink[1], Anton Korosov[2], Thomas Newman[3], Andreas Theodosiou[1], Yuanhao Li[1], Gert Mulder[1], Pierre Rampal[2], Julienne Stroeve[3], and Paco Lopez-Dekker[1]

[1]Geoscience and Remote Sensing, Delft University of Technology
[2]Nansen Environmental and Remote Sensing Center
[3]Centre for Polar Observation and Modelling, University College London

Correspondence: Marcel Kleinherenbrink (m.kleinherenbrink@tudelft.nl), Paco Lopez-Dekker (f.lopezdekker@tudelft.nl)

Abstract. This article describes the observation techniques and processing methods to estimate dynamical sea-ice parameters from data of the Earth Explorer 10 candidate Harmony. The two Harmony satellites will fly in a reconfigurable formation with Sentinel-1D. Both will be equipped with a multi-angle thermal infra-red sensor and a passive radar receiver, which receive the reflected Sentinel-1D signals using two antennas. During the lifetime of the mission, two different formations will be flown. In the stereo formation, the Harmony satellites will fly approximately 300 km in front and behind Sentinel-1, which allows the estimation of instantaneous sea-ice drift vectors. We demonstrate that the addition of instantaneous sea-ice drift estimates on top of the daily integrated values from speckle tracking have benefits in terms of interpretation, sampling and resolution. Additionally, it allows for the extraction of deformation parameters, such as shear and divergence. As a result, Harmony's data will help improve sea-ice statistics and parametrizations to constrain sea-ice models. In the cross-track interferometry (XTI) mode, Harmony's satellites will fly in close formation with an XTI baseline to be able to estimate surface elevations. This will allow for improved estimates of sea-ice volume, and also enable for the first time to retrieve full two-dimensional swell-wave spectra in sea-ice covered regions without any gap. In stereo formation, the line-of-sight diversity allows to get swell in both directions using traditional velocity bunching approaches. In XTI mode, Harmony's phase differences are only sensitive to the ground-range direction swell. To fully recover two-dimensional swell-wave spectra, a synergy between XTI height spectra and intensity spectra is required. If selected, the Harmony mission will be launched in 2028.

1 Introduction

Sea ice plays a vital role in the climate system, reflecting sunlight and acting as an insulator between the ocean and the atmosphere. It also provides an important habitat for marine biota and serves as a platform for coastal populations (Krupnik, I. et al., 2010; Dammann et al., 2019). Reductions in sea-ice area and volume therefore have local as well as global impacts and requires careful monitoring. Satellites play a key role in this monitoring, and have documented large-scale reductions in Arctic sea-ice extent year round since the late 1970s (Stroeve and Notz, 2018), and support climate model simulations that the

https://doi.org/10.5194/tc-2020-245
Preprint. Discussion started: 30 October 2020

Arctic will likely transition towards seasonally ice-free conditions before the middle of this century as a result of increases in atmospheric greenhouse gases (Notz et al., 2020). In contrast, over the same time-period, Antarctic sea-ice extent has exhibited slight positive increases until 2014 when ice conditions started to reduce, highlighting the strong influence of natural climate variability in this region (Parkinson, 2019). While satellites have monitored large-scale sea ice extent for more than 40 years, sea-ice thickness on a large-scale was only sampled sporadically in the 2000s from ICESat (Lindsay and Schweiger, 2015) and is currently monitored using both CryoSat-2 and ICESat-2 (Ricker et al., 2017). Nevertheless, this data has suggested an overall decline in Arctic sea-thickness and hence total ice volume (Ricker et al., 2014; Armitage and Ridout, 2015), while thickness trends in the Antarctic remain uncertain (Price et al., 2019).

Even though large-scale trends in extent and thickness are apparent, the processes governing regional sea-ice changes remain poorly observed. Most of the regional processes that cause changes in sea-ice volume are related to sea-ice drift. Small-scale volume changes are the direct effect of changes in the net drift of sea ice into an area, which is primarily driven by ocean currents and wind stress. Indirectly, sea-ice drift opens leads, which exposes the warm sea water to the colder atmosphere, and the formation of pressure ridges, which act like sails and keels for the atmosphere and ocean to exert forces upon. Observations of sea-ice drift are made from a variety of spaceborne instruments, like scatterometers, side-looking radars and optical sensors, as well as terrestrial observations from drifting buoys (Sumata et al., 2014; Long, 2017). Spaceborne Synthetic Aperture Radar (SAR) provides, with the use of methods like speckle tracking, high-resolution observations, while covering the both poles without any gaps. The speckle-tracking approach allows for integrated values obtained between two satellite overpasses, at a sampling rate that depends on latitude, but is typically once per day. Daily integrated values however undersample the sea-ice dynamics and lead to an underestimation of the drift speeds (Haller et al., 2014; Dammann et al., 2019). This is particularly true for breakup events, where the instantaneous velocities are an order larger than the daily averages. The application of SAR to estimate drift velocities in marginal ice zones is also limited, due to the difficulty of tracking the more dynamic small ice floes.

Ardhuin et al. (2017) and Stopa et al. (2018) demonstrated the estimation of wave spectra using SAR in sea-ice covered regions. The approach exploits the phenomenon of velocity bunching, which is the displacement of scatterers in the azimuth direction of the SAR image as a consequence of the motions of swell waves in the range direction. Velocity bunching does not occur when waves travel in the range direction, so to obtain gap-free two-dimensional swell-wave spectra requires ascending and descending passes and the assumption that between those satellite passes the spectrum does not change. The spectra are further contaminated by sea-ice features e.g., ridges, that cover a similar spectrum as the swell waves (Ardhuin et al., 2017). Some processes, like fracturing of floes are related to the penetration of long-wavelength ocean waves into the sea ice (Squire, 2018). As only a few limited studies have been performed to observe swell-wave dissipation in sea-ice-covered regions, this is currently poorly constrained in models. Using Sentinel-1 it is possible to estimate swell spectra over 5 km $\times$ 7 km regions based on a modulation of the amplitude in SAR images caused by swell waves. However, swell waves that propagate in the cross-track direction are not visible (Stopa et al., 2018).

The proposed bi-static Harmony SAR mission aims to provide new data for a wide range of applications, such as ocean-atmosphere interaction, hurricanes, solid Earth and land ice studies (López-Dekker et al., 2019). Harmony has also the capabil-

https://doi.org/10.5194/tc-2020-245
Preprint. Discussion started: 30 October 2020

ity to overcome several limitations of current sea-ice observing systems. The Earth Explorer 10 candidate mission consists of two companion satellites (Concordia and Discordia), which will fly in formation with one of the Sentinel-1 satellites (from here on it is assumed to be Sentinel-1D). The satellites will carry a multi-angle thermal infrared senor and two passive instruments that will receive signals from a scene illuminated by the radar of Sentinel-1D. In the stereo phase of the mission, the Harmony satellites are trailing and leading Sentinel-1D, which creates line-of-sight diversity. A two-channel receiver system onboard the satellites allows the radial velocity component of the surface to be retrieved, which in combination with the line-of-sight diversity enables the estimation of instantaneous two-dimensional velocity fields, which in case of polar waters is sea-ice drift. In cross-track interferometry (XTI) mission phases, the Harmony satellites fly in a close formation with a cross-track or radial baseline of several hundreds of meters. The observed phase differences between the two receivers are a result of surface topography, from which swell-wave properties can be inferred. This is something not possible with two monostatic systems, nor with repeat-pass interferometry due the decorrelation of the surface.

The objective behind this article is to describe the expected performance and the application of the Harmony mission for sea-ice dynamics i.e., sea-ice drift and waves. Harmony data also enables estimates of sea-ice topography, but this will not be addressed in this paper. We will introduce the bi-static geometry and the observation concept and show how to derive sea-ice drift fields from the stereo configuration and wave spectra in both the stereo and XTI configurations. Harmony observations are modelled based upon sea-ice drift estimates from a sea-ice model and noise is added using electromagnetic models for the noise-equivalent sigma zero (NESZ) and the backscatter coefficient over sea-ice. We will discuss the performance in terms of accuracy, resolution and sampling. With dedicated filters and edge detection algorithms, it is further shown that the data from Harmony is suited for the estimation of deformation parameters, like shear and divergence. As a final step, we demonstrate how wave-spectra can be retrieved based on end-to-end simulator and argue that Harmony is able to retrieve two-dimensional wave spectra in both formations.

1.1 Harmony's observation geometry

This paper does not attempt to detail the baselines over the orbit, but assumes realistic values wherever necessary to compute the performance of Harmony. A detailed overview of the observation geometry of Harmony will be discussed in a separate publication. Figure 1 shows the reconfigurable formation of Harmony. By several orbit manoeuvres Harmony-B, or Discordia, can be moved from the stereo to the XTI position, which typically takes one to two months. In the expected mission lifetime of five years, Harmony will fly approximately two years in the XTI formation and three years in the stereo formation.

As visible in figure 1, both satellites carry a passive radar instrument that receives the C-band echoes from the swath illuminated by Sentinel-1D at two antennas, separated several meters in the along-track direction. The two phase centers can be used as a single receiver to get improved radiometric performance, or as two separate receivers to allow for short-baseline along-track interferometry (ATI). The phases differences of ATI are a result of range direction motion of the surface in the effective time separation between the antennas, which is related to the effective along-track separation of the antennas and the platform velocity. The effective along-track separation differs from the physical baseline between the two phase centers as the satellites have to be slanted to point the beams towards the illuminated swath. Since the stereo formation has two-lines of

https://doi.org/10.5194/tc-2020-245
Preprint. Discussion started: 30 October 2020

sight, the ground motion will be observed in two directions, allowing for the separation of azimuth and cross-track direction of sea-ice drift.

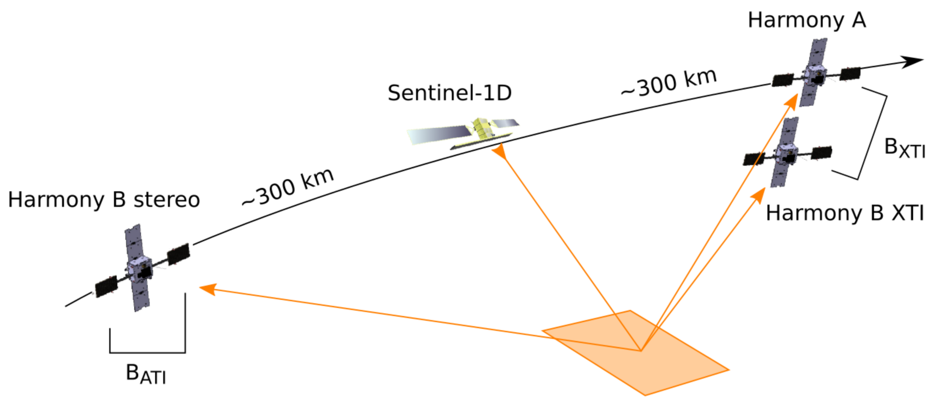

Figure 1. The reconfigurable configuration of the Harmony-Sentinel-1 constellation. In the stereo formation one of the Harmony satellites trails Sentinel-1 and the other heads Sentinel-1. In the XTI configuration, the Harmony satellites fly in close formation. Adapted from Kleinherenbrink, M. et al. (2019).

In the close formation, inter-satellite interferogrammetry can be applied, which makes the phase sensitive to motion if there is an effective along-track separation, or height, if there is an effective cross-track baseline. The range difference depends on the receiver positions only for XTI, the effective baseline to estimate elevation is in the plane of the received signal. The slanted geometry of Harmony allows to minimize the inter-satellite ATI baseline, but variations over the orbit occur, which makes the phase sensitive to ground motion. To separate ground motion from topography, short-baseline ATI between the two phase centers on one satellite is used to determine the ground-range motion. If high radiometric performance is required and both phase antennas are used to form a single phase center, methods like Doppler centroid anomaly estimation could be used (Madsen, 1989). Doppler centroid estimation has an inferior accuracy with respect to short-baseline ATI and puts requirements on the surface i.e., strong variations in NRCS over the scene would introduce biases.

While the bi-static nature of Harmony provides the opportunity for estimating instantaneous two-dimensional velocities and instantaneous elevations, there are some observational consequences. ATI and XTI phase difference are a factor of two smaller than in interferograms computed from overpasses of two monostatic systems, because there is only one transmitter and two receivers. Additionally, the slant of the receivers cause a rotation of the observed polarization. The coherent geometrical polarization change is predictable and can be anticipated, either in the design or in the processing of the data. The non-coherent part reflects the change of polarization in different lines-of-sight, and will provide additional information about the geometry of the surface, like directional ocean waves. Finally, as will be discussed in section 3, waves modulate the amplitudes depending on their orientation with respect to the transmitter-receiver system. This will make Harmony sensitive to all directions of swell.

2 Methods

The performance of Harmony's potential for sea-ice-drift observations is analysed with the use of a neXtSIM sea-ice model. From the model input, the noise-free multilooked ATI phases are computed and noise is added using electromagnetic models for the backscatter and the NESZ. After addition of noise, the process is reversed to get an estimate of Harmony's surface velocity estimates. Filtering and edge detection methods are suggested to de-noise the velocity fields, while keeping discontinuities intact. We additionally describe an OceanSAR end-to-end model, which is used to simulate radar signals from swell waves in sea-ice-covered waters and demonstrate the ability of Harmony to recover swell signals based on both XTI and stereo phase and amplitude spectra.

2.1 Sea-ice model

If launched, Harmony will be the first mission that is able to reveal instantaneous deformation patterns, like shear stresses and convergence near discontinuities. To be able to simulate Harmony's performance, we take our input sea-ice dynamics from the latest version of the Lagrangian neXtSIM model (Rampal et al., 2019). The elasto-brittle model is much better able to capture sea-ice drift and deformation statistics as compared to classical elasto-viscous-plastic models (Rampal et al., 2016). A pan-Arctic with a time-step of 200 seconds and a horizontal resolution of approximately 3.5 km x 3.5 km. The stereographic coordinates and velocities have been converted to ground-projected radar coordinates and velocities, and then interpolated to the resolution set by the experiments in the later sections. A median filter is applied to remove interpolation effects by the conversion from a triangular to a Cartesian grid, while keeping the discontinuities intact.

2.2 Phase measurements

The radial velocity of the surface can be measured by two acquisitions of the surface separated in time. ATI makes use of the phase difference caused by a time offset between the two coinciding Doppler centroids i.e., after processing the signals received at the two antennas can be considered as two acquisitions of the same scene separated by a time difference Δt. In case of a monostatic systems, this is directly related to the along-track baseline, such that the time difference is given as

$$\Delta t_m = \frac{B_{ATI}}{V_{sat}}, \tag{1}$$

where V_{sat} is the platform velocity. In a bi-static system, like Harmony, where there is one transmitter and two receivers, the Doppler Centroid moves only half the baseline distance, which results in an effective time difference of

$$\Delta t_b = \frac{B_{ATI}}{2V_{sat}}. \tag{2}$$

The Doppler shift measured by Harmony is, in contrast to standard monostatic systems, not only sensitive to across-track surface velocity v, but also to its along-track component u. Using the orientation and geometry described in the previous section, the Doppler is given by Kleinherenbrink, M. et al. (2019)

$$f_{D,\pm} = \pm\frac{\sin(\theta_r)\sin(\alpha_b)}{\lambda_0}\cdot u - \frac{\sin(\theta_i)+\sin(\theta_r)\cos(\alpha_b)}{\lambda_0}\cdot v, \tag{3}$$

https://doi.org/10.5194/tc-2020-245
Preprint. Discussion started: 30 October 2020

where $\pm$ is negative for Discordia and is positive for Concordia. The phase difference caused by surface velocities is computed as Duque et al. (2010)

$$\Phi_{ATI,\pm} = 2\pi \cdot f_{\mathrm{D}} \cdot \Delta t_b. \tag{4}$$

From equation 3 it follows that the along-track velocity can be reconstructed by subtracting the phase differences of Concordia and Discordia and the cross-track velocity by a summation under the assumption that the distance between Sentinel-1 and the two Harmony satellites is equal. Then we can write

$$\begin{aligned}\hat{u} &= \frac{\lambda_0}{2\pi\Delta t_b}\frac{\hat{\Phi}_{ATI,+} - \hat{\Phi}_{ATI,-}}{2\sin(\theta_r)\sin(\alpha_b)}\\ \hat{v} &= -\frac{\lambda_0}{2\pi\Delta t_b}\frac{\hat{\Phi}_{ATI,+} + \hat{\Phi}_{ATI,-}}{2(\sin(\theta_i) + \sin(\theta_r)\cos(\alpha_b))}\end{aligned} \tag{5}$$

for the velocity estimates, where $\hat{\Phi}_{ATI,\pm}$ are the observed phases.

Height sensitivity in SAR is achieved by using acquisitions of the same scene separated by cross-track distance. In side-looking monostatic systems, the two-way range difference between two passes can directly be coupled to surface elevation. For Harmony the same is true, except that it only depends on a single-way range difference as there is only one transmitter and two receivers in a cross-track formation. Note that in case of a bi-static system, the effective XTI baseline B_{XTI} is also not in the cross-track direction, but along the line-of-sight of the receivers. The height of ambiguity is given by

$$H_a = -\frac{\lambda r_1 \sin(\theta_r)}{B_{XTI} * \cos(\theta_r - \alpha)} \tag{6}$$

with r_1 the range toward one of the receivers and α is the slope angle of the XTI baseline. Then the interferometric phase difference caused by topography h is computed with

$$\Phi_{XTI} = 2\pi\frac{h}{H_a}. \tag{7}$$

2.3 Noise modelling and bi-static backscatter

Realistic values for retrieved velocities and elevations are obtained by adding noise to the forward-modelled interferometric phases. The interferometric phase noise is related to the coherence γ and is computed as (Dierking et al., 2017; Rosen et al., 2000)

$$\sigma_{phi} = \sqrt{\frac{1-\gamma^2}{2N\gamma^2}}, \tag{8}$$

where N is the number of independent looks. Using the equations from section 2.2, the phase noise is converted to velocity and elevation noise. For the computation of the phase noise, the coherence γ is modelled, which is by a multiplication of several different parts, such that

$$\gamma = \gamma_{sys} \cdot \gamma_{XT} \cdot \gamma_{AT} \cdot \gamma_{vol}, \tag{9}$$

https://doi.org/10.5194/tc-2020-245
Preprint. Discussion started: 30 October 2020

where γ_{sys}, γ_{XT} and γ_{AT}, respresent the system coherence and the range and along-track baseline decorrelation, respectively. The term γ_{vol} related to volume decorrelation is set to 1.

In the close formation, inter-satellite phase difference are computed, so that the along-track and cross-track baselines cause significant changes to the spectra. In Stereo formation, where we use a separation of a few meters between the phase centers, it is possible to ignore baseline decorrelation. The decorrelation caused by these spectral shifts is related to the critical baselines in both directions. In the range direction the critical baseline is given as

$$B_{XTI,crit} = \frac{\lambda_0 a}{\Lambda_{ra}\cos^2(\theta)}, \tag{10}$$

whereas

$$B_{ATI,crit} = \frac{\lambda_0 a \cos(\theta)}{\Lambda_{az}\sin(\theta)} \tag{11}$$

is the along-track critical baseline, with a the satellite altitude, and Λ_{az} and Λ_{ra} the resolution in the azimuth and range directions, respectively. The combination of both baselines, B_{ATI} and B_{XTI}, yields a coherence of (Dierking et al., 2017)

$$\begin{aligned} \gamma_{XT} &= 1 - \frac{B_{XTI}}{B_{XTI,crit}} \\ \gamma_{AT} &= 1 - \frac{B_{ATI}}{B_{ATI,crit}}\ . \end{aligned} \tag{12}$$

The system coherence depends on the Signal-to-Noise Ratio (SNR), which in itself depends on the backscatter coefficients σ_0 and the Noise Equivalent Sigma Zero (NESZ), such that

$$SNR = \frac{\sigma_0}{\mathrm{NESZ}}. \tag{13}$$

Then the corresponding coherence is given by

$$\gamma_{sys} = (1 + \frac{1}{\mathrm{SNR}})^{-1} \tag{14}$$

The NESZ depends on the system parameters and the antenna gains of both Sentinel-1 and Harmony. If both phase centers onboard the Harmony satellites are used as a single antenna, a better radiometric performance is achieved. In case of short-baseline ATI, both phase centers are used separately, causing the beam to widen and the NESZ to increase. The NESZ can be computed using

$$\mathrm{NESZ} = \frac{E_n}{E_s}, \tag{15}$$

with

$$E_n = kT_{sys}BW, \tag{16}$$

where BW is the bandwidth, T_{sys} the noise temperature and k Boltzmann's constant. The received signal energy as a function of the transmitted energy E_p is given by the radar equation

$$E_s = E_p(p_{2w}\frac{\lambda}{(4\pi)^{1.5}r_1^2}\sqrt{A_{res}}G_{0,tx}G_{0,rx})^2, \tag{17}$$

https://doi.org/10.5194/tc-2020-245
Preprint. Discussion started: 30 October 2020

with p_2w the two-way antenna pattern A_res the resolution and $G_{0,tx}$ and $G_{0,rx}$ the maximum transmitter and receiver gains, respectively. The antenna patterns are computed for two 0.7 m × 3.2 m separated by approximately 9 m, which are approximate dimensions set by preliminary feasibility studies from industry. For the single phase center Harmony receiver, the NESZ varies over the swath (figure 2) and has typical values of -22 dB.

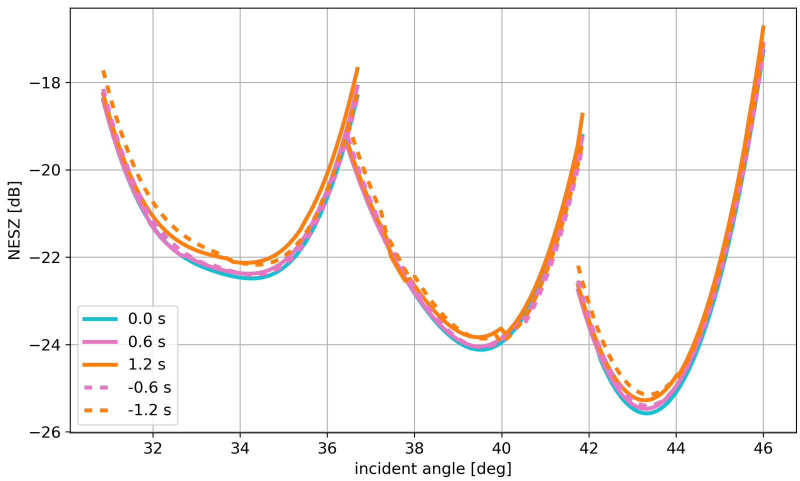

Figure 2. The estimated NESZ for Harmony for three azimuth locations: at zero Doppler (0.0 s),at about 5 km from the zero Doppler (0.6 s) and at about 10 km from zero Doppler (1.2 s). The subswath edges of Sentinel-1's IW mode are visible by the discontinuities.

The backscatter coefficient depends on the incidence angle, the ice type and the roughness of the surface. Dierking et al. (2017) summarized the range of backscattering coefficients for various types of sea ice based on previous studies. Many analyses of the backscatter coefficient have been performed over various types of ice (Kwok and Cunningham, 1994; Dierking, 2010; Ulaby and Long, 2015). C-band backscattering coefficients typically ranged from -23 to -8 dB for monostatic systems. bi-static estimates in C-band have not been made so far, so we rely on a two-layer implementation (snow and sea ice) of the model of Komarov et al. (2014) and Komarov et al. (2015). The backscatter coefficients at the interfaces for polarization xx are summed to get total backscatter coefficient, such that:

$$\sigma_{xx} = \sigma_{xx,air-snow} + \sigma_{xx,snow-ice}. \tag{18}$$

Over sea ice Sentinel-1 transmits signals in a horizontal polarization and Harmony receives in both polarizations. Therefore only the two equations for HH and HV are required, which depend on the incoming incidence and azimuth angle (θ_i,ϕ_i) and the reflected angles (θ_r,ϕ_r). Let $q_{i,r}$ be the wave vectors for the incoming and reflected signals as in Komarov et al. (2014). The backscatter coefficient in HH for the air-snow interface is computed as

$$\sigma_{HH,air-snow} = \frac{k_0^4|\Delta\epsilon_{as}|^2}{4\pi}|[1+R_H(q_i)][1+R_H(q_r)]|^2\cos^2(\phi_r-\phi_i)K_s(q_r-q_i) \tag{19}$$

https://doi.org/10.5194/tc-2020-245
Preprint. Discussion started: 30 October 2020

and for the snow-ice interface as

$$\sigma_{HH,snow-ice} = \frac{k_0^4|\Delta\epsilon_{si}|^2}{4\pi}|L_H(q_i)L_H(q_r)|^2\cos^2(\phi_r-\phi_i)K_i(q_r-q_i). \tag{20}$$

The cross-polarization terms HV are computed with

$$\sigma_{HV,air-snow} = \frac{k_0^4|\Delta\epsilon_{as}|^2}{4\pi}|[1+R_H(q_i)][1-R_V(q_r)]\sin(\phi_r-\phi_i)\cos(\theta_r)|^2K_s(q_r-q_i) \tag{21}$$

and

$$\sigma_{HV,snow-ice} = \frac{k_0^4|\Delta\epsilon_{si}|^2}{4\pi}|L_H(q_i)M_V(q_r)|^2\sin^2(\phi_r-\phi_i)K_i(q_r-q_i). \tag{22}$$

In the above equations $\Delta\epsilon_{as}$ and $\Delta\epsilon_{si}$ are the differences between the air and snow dielectric coefficients and the snow and ice dielectric coefficients, respectively. The spatial spectra of the air-snow $K_s(q_r-q_i)$ and the snow-ice $K_i(q_r-q_i)$ interface are considered to be uniform, and therefore we take them as (Komarov et al., 2015)

$$K_{s,i}(|q_r-q_i|) = \frac{2\pi L_{s,i}^2\sigma_{s,i}^2}{(1+|q_r-q_i|^2L_{s,i}^2)^{1.5}}, \tag{23}$$

where $L_{s,i}$ are the correlation lengths and $\sigma_{s,i}$ the roughness of the interfaces. Using the scheme in the appendix of Komarov et al. (2015), the reflection coefficients $R_H(q_{i,r})$ and $R_V(q_{i,r})$ are computed, such that

$$R_H(q_{i,r}) = r_{d,H}^{0,1}(q_{i,r}) + \frac{t_{d,H}^{0,1}(q_{i,r})t_{u,H}^{0,1}(q_{i,r})r_{d,H}^{1,2}(q_{i,r})u_1^2}{1-r_{u,H}^{0,1}(q_{i,r})r_{d,H}^{1,2}(q_{i,r})u_1^2} \tag{24}$$

and

$$R_V(q_{i,r}) = r_{d,V}^{0,1}(q_{i,r}) + \frac{t_{d,V}^{0,1}(q_{i,r})t_{u,V}^{0,1}(q_{i,r})r_{d,V}^{1,2}(q_{i,r})u_1^2}{1-r_{u,V}^{0,1}(q_{i,r})r_{d,V}^{1,2}(q_{i,r})u_1^2}, \tag{25}$$

with t,r the Fresnel transmission and reflection coefficients, u,d indicating upward or downward, H,V the polarization and $0,1,2$ the air, snow and ice layers, respectively. For example $t_{u,H}^{0,1}(q_i)$ is the upward Fresnel coefficient of the incoming signal for the air-snow interface for the horizontal polarization. The factor u_1 represents a phase change through the snow layer with thickness Δz and is given by

$$u_1 = exp(i\omega_1\Delta z), \tag{26}$$

where ϵ_s is the dielectric constant of the snow layer and

$$\omega_1 = k_0\sqrt{\epsilon_s - \sin^2\theta_i} \tag{27}$$

is the projection of the wave vector onto the z-axis in the snow layer. The two auxiliary variables L_H and M_V as given in the backscatter equation are given using the notations in the same scheme, such that

$$L_H(q_{i,r}) = \frac{\omega_0(q_{i,r})}{\omega_1(q_{i,r})}\frac{t_{u,H}^{0,1}(q_{i,r})u_1}{1+r_{d,H}^{1,2}(q_{i,r})\cdot r_{d,H}^{0,1}(q_{i,r})\cdot u_1^2}[1+r_{d,H}^{1,2}(q_{i,r})] \tag{28}$$

and

$$M_V(q_{i,r}) = \frac{\omega_0(q_{i,r})}{k_0} \frac{t^{0,1}_{u,V}(q_{i,r})u_1}{1 + r^{1,2}_{d,V}(q_{i,r}) \cdot r^{0,1}_{d,V}(q_{i,r}) \cdot u_1^2}[1 - r^{1,2}_{d,V}(q_{i,r})]. \tag{29}$$

The term ω_0 is the projection of the wave vector onto the z-axis in air, such that

$$\omega_1 = k_0\sqrt{1 - \sin^2\theta_i}. \tag{30}$$

2.4 Post-processing

To be able to derive accurate deformation parameters near the discontinuities (e.g., shear and pressure zones), averaging should be applied parrallel and not perdendicular to these features. However, the identification of these structures is non-trivial, because even after some multilooking the noise might be large enough to cover the discontinuities. To demonstrate that it is indeed possible to indentify the gradients, we designed a two-step solution, which comprises of a variant of the Wiener filter and an edge detection method. The adaptive Wiener filter ensures that the scenes becomes interpretable and that the noise is suppressed, while maintaining the sharp gradients. With the edge detection method, the gradients in velocity are detected, so that consecutively suitable averaging methods can be applied to compute the instanteneous pressure and shear. Note that the method described here is only one of the possible processing flows. Other, more advanced methods, can be developed once Harmony is delivering data. The settings and thresholds used in the described method can also be varied, depending on the application.

As the backscatter coefficient and NESZ are known, an estimate can be made of the velocity noise σ_n. Under the assumption that 1 km $\times$ 1 km multi-looking is applied, speckle is suppressed and the velocity noise is considered to be Gaussian. Using a two-dimensional discrete Fourier transform of the along- or across-track velocity field $V_{u,v}$, the PSD is computed as

$$\Phi_{u,v} = \frac{|V_{u,v}|^2}{N \cdot M}, \tag{31}$$

where N and M are the dimensions of the velocity field. Unfortunately, the spectrum of the true velocity field are not known, so therefore we make an estimate, such that:

$$\Phi_{(u,v),true} = \Phi_{u,v} - s\sigma_n^2, \tag{32}$$

where s is a scale factor for the noise. Negative values for $\Phi_{(u,v),true}$ cannot exist, so they are set to 0. Our adaptive Wiener filter is then given as:

$$W = \frac{\Phi_{(u,v),true}}{\Phi_{u,v}}, \tag{33}$$

so that our filtered velocity fields in the frequency domain read

$$V_{(u,v),f} = WV_{u,v}. \tag{34}$$

Even though the noise is suppressed by the Wiener filter, we find that standard edge detection methods, such as the Canny edge detector, are not suitable. Therefore, we opt for an alternative involving multiple neighbouring pixels. To detect potential

https://doi.org/10.5194/tc-2020-245
Preprint. Discussion started: 30 October 2020

edges in the azimuth and ground-range direction, we convolve the Wiener filtered fields with edge-detection filters of size N × 2N and 2N × N of which one half contains the values $\frac{-1}{N^2}$ and one half $\frac{1}{N^2}$. The size of N is varied from 6 to 14 pixels with a step of 2, and the resulting fields are multiplied. This has the goal to minize false detections away from the edges (this is done by the larger filters), while getting a precise location of the edge (this is done by the smaller filters). Peaks in the resulting field are detected by an algorithm that scans the filtered velocity fields line-by-line. This operation is applied four times: for the u and v components and for discontinuities in both directions.

To fix edges that are broken, a binary image of potential edge locations is created and dilated. Regions identified as potential edges are kept if they have more than 50 pixels connected together in the dilated binary images. Then to sharpen the edges again, the binary image is eroded. For every remaining edge location, the edge-detection filter with size N=10 is applied and the resolution of Harmony's output velocity field is used to determine the gradient. Using the gradients, we determine the absolute value of the shear as

$$\tau = \sqrt{(\frac{dv}{dx})^2 + (\frac{du}{dy})^2}, \tag{35}$$

and the divergence as

$$\nabla = \frac{du}{dx} + \frac{dv}{dy}. \tag{36}$$

2.5 Wave spectra

The software package OceanSAR is used to demonstrate Harmony's ability to measure swell waves in sea-ice-covered regions. Harmony data can be used in two ways to extract wave spectra. If Harmony flies in the XTI configuration, the phase differences between the two satellite systems are a direct measure for the height. In both the XTI and Stereo formations, the image distortions due to velocity bunching provides a way of inferring wave information from intensity spectra. To the first order, a bi-static observation can be modelled as a mono-static system located at the midpoint between the transmitter and receiver. In this paper, we consider a system of one transmitter and two receivers (XTI mode), so that we have a monostatic and a bi-static system of which the bi-static receiver is located across track. This also implies that both systems have a common zero-Doppler, which makes the interpretation easier. Using OceanSAR, the RAW signals are modelled using scatterers at a 2 m resolution Lagrangian grid i.e., the swell waves cause three-dimensional changes to the surface during the burst. As the small waves are quickly damped by the sea ice (Stopa et al., 2018), the surface is assumed to be correlated over the burst length. The average SNR is set to approximately 5 dB and the bi-static baseline to 1000 m.

The data is then focused, and has a comparable resolution as the Sentinel-1's IW mode. From the single-look complex images intensities and interferometric phases are computed. These are multilooked using a Hanning window with a size of 12 × 4, which yields a resolution of about 65 m × 65 m, since the simulated resolution is approximately 16 meter in azimuth and 5 m in the ground-range direction. Using the equation for the height of ambiguity in section 2.2, the surface elevation is computed from the phases. Spectra are estimated using Bartlett's method, using eight non-overlapping patches over the 4 km × 4 km grid. Finally, by squaring the mean periodogram and scaling it by the number of samples the amplitude spectrum is computed.

https://doi.org/10.5194/tc-2020-245
Preprint. Discussion started: 30 October 2020

3 Discussion of the results

The measurements of Harmony and its characteristics are addressed in four sections. The first section discusses the expected SNR and the overall performance of the system for surface velocity vector estimation from Harmony data. Then we address the coverage in terms of the number of passes and the expected accuracy in each pass. The third section focuses on strategies to reveal structure and estimate accurate gradients. Finally, we have a separate discussion on the estimation of wave spectra from intensity images and XTI elevations.

3.1 Performance metrics

An estimate of the bi-static NRCS is required to compute the performance of Harmony. As mentioned before, based on other studies the backscatter coefficient of sea ice typically ranges from -23 to -8 dB, depending on the surface properties and the incidence angle. These numbers are used to constrain the snow and ice properties, which are input for the model. The backscatter is then computed as a function of bi-static angle and incidence angle (figure 3). In the right panel, the monostatic case is plotted for reference. The monostatic backscatter shows a typical decay with incidence angle, which is similar to the patterns observed in Sentinel-1, ESA's ICESar campaign and the study of Komarov et al. (2015). Volume scattering is often small for sea ice (Komarov et al., 2015) and is not modelled, hence the HV component is nearly zero. Therefore, the coherent sum of the HH and HV backscatter is approximately equal to the magnitude of HH. Note that volume scattering is not always negligible, for example over deformation features or multiyear ice (Scheuchl et al., 2005; Shokr, 2009). The curving behavior of the solid line is a result of interference between the signals reflecting from the two interfaces and depends on the snow thickness. In the reality this behavior is unlikely as snow bedforms modulate snow thickness over a multitude of scales (Filhol and Sturm, 2015).

The middle panel shows that a similar pattern is visible for the coherent sum of the backscatter in the bi-static case. However, the ratio between the HH and HV have changed as a consequence of the change in geometry. This is further illustrated by the left panel, where it shown that the ratio HV-HH increases with increasing ground-projected bi-static angle. Note that towards the end of the swath the the incidence angle increases, while the bi-static angle decreases, which causes the HV component to be more prominent at the near-field than at the far-field. The coherent sum the backscatter only decreases slightly with increasing bi-static distance, hence the descrease in SNR is small. This result depends on the surface properties, but is fairly robust.

Under the assumption of that the loss backscatter for the bi-static is small with respect to a monostatic system, the performance of Harmony is computed for a range of SNRs (figure 4). At the considered 1 km $\times$ 1 km multilook (left panel) usable velocity estimates in both directions are expected at a SNR of 0 dB in Sentinel-1D's IW mode, because typical ice-drift velocities are below 0.5 m s^{-1} (Scheiber et al., 2011; Dierking et al., 2017; Dammann et al., 2019). In the worst-case scenario, at an SNR of -5 dB, a resolution of 2 km is sufficient to extract information about the fastest ice floes using Sentinel-1D's IW mode. For a typical situation with 5 dB SNR a substantial fraction of the sea-ice drift is resolved at 1 km x 1 km resolution. The accuracy changes over the swath, which is caused by the aforementioned variation in incidence and bi-static angles (right

https://doi.org/10.5194/tc-2020-245
Preprint. Discussion started: 30 October 2020

The Cryosphere
Discussions
Open Access

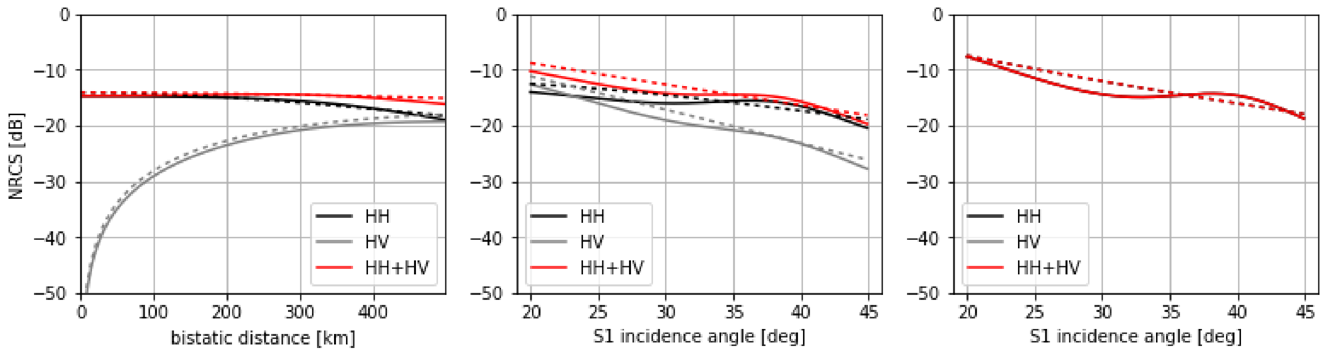

Figure 3. Plots of the modelled NRCS for the HH and HV polarizations as a function of bi-static distance (left) and the Sentinel-1 incidence angle (middle: bi-static case, right: monostatic case), while keeping along-track distance between Harmony and Sentinel-1 at 300 km. The solid lines correspond to a snow-covered ice surface and the dashed lines a snow-free scene. The dielectric constants are set to 1.5 and 3.6 for snow and ice, the surface roughness to 0.5 cm and the correlation length to 2 cm for both interfaces. These values are in agreement with Komarov et al. (2015) and Landy et al. (2019). The snow thickness is set to 20 cm.

panel). Under the assumption of a constant SNR over the swath, this leads to an improved cross-track accuracy and a slightly decreased along-track accuracy. To achieve similar accuracy at least 4 km $\times$ 4 km of averaging is required when operating Sentinel-1D in the EW mode (middle panel), which is the current operating mode over most of the polar areas. A change of operational mode will therefore be beneficial for sea-ice studies.

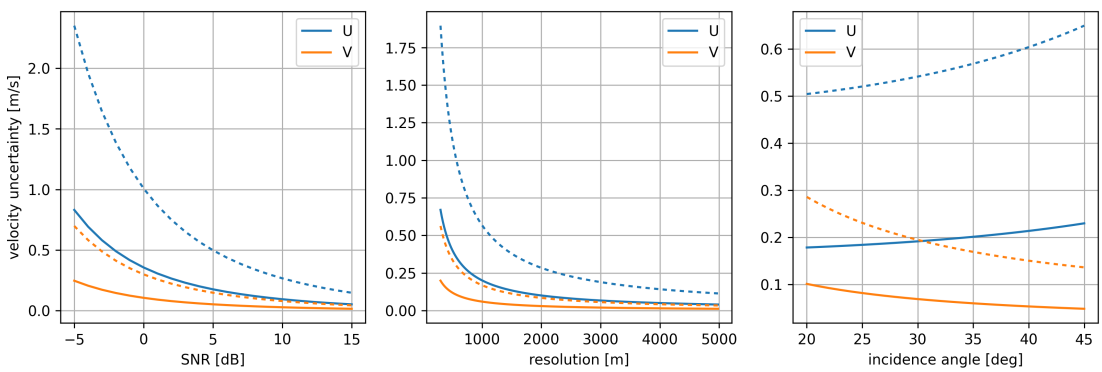

Figure 4. Modelled velocity uncertainties based on a flat Earth approximation. U and V represent the along- and across-track velocity uncertainties, respectively. The solid lines represent the performance for the IW mode, while the dashed line represent the performance for the EW mode. In the left panel the resolution is kept constant at 1 km $\times$ 1 km and in the middle panel the SNR is kept constant at 4 dB. The baseline between the two phase centers is set to 9 m and the incidence angle of Sentinel-1 to 35°. The distance between the Harmony satellites and Sentinel-1 is kept constant at 300 km. In the right panel, all of the previously mentioned settings are used to show the variations over the incidence angle.

https://doi.org/10.5194/tc-2020-245
Preprint. Discussion started: 30 October 2020

The Cryosphere
Discussions
Open Access

3.2 Coverage and sampling

The wide swath of Sentinel-1D's EW mode was requested by the sea-ice community to increase the sampling rate for speckle tracking algorithms to estimate sea-ice velocity. For the operation of Harmony, Sentinel-1D's IW mode is prefered, because of the enhanced number of independent looks, which allows to suppress the noise of velocity estimates. As the number of SAR mission increases and likely three Sentinel-1 satellites will be operated at the moment of launch, a request will likely be made to operate Sentinel-1D in IW mode over at least part of the sea ice. Therefore we will discuss both the coverage in the IW and the EW mode.

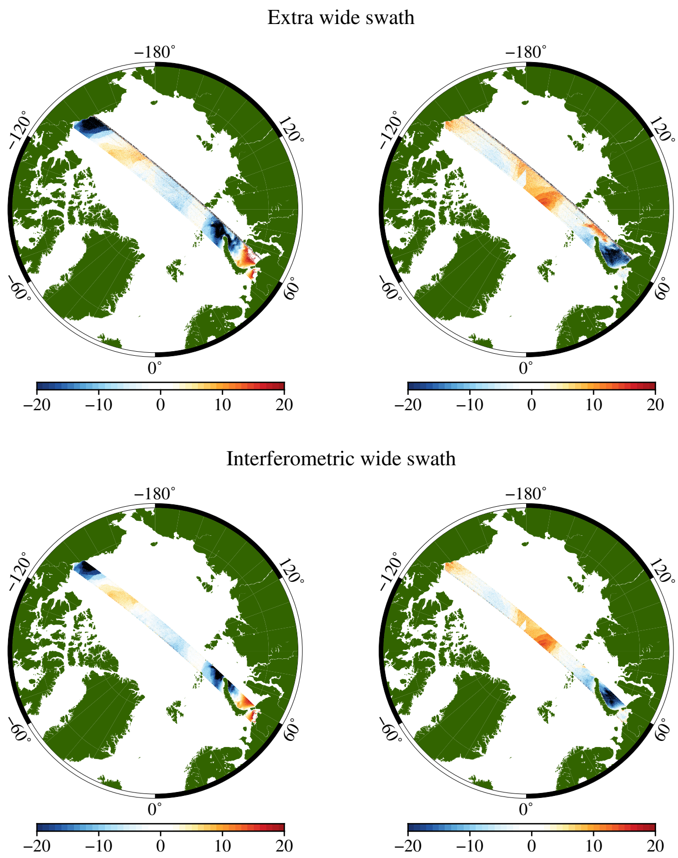

Figure 5. Modelled sea-ice velocity (cm s^{-1}) observations for a single pass of Harmony in the East (left) and North (right) directions for the EW and IW modes. The swath of the EW is clearly wider, which increases the temporal sampling at the costs of resolution.

Figure 5 shows the estimated velocity from Harmony based on the input data from the neXtSIM model. The swath of the currently operated EW mode is with about 400 km about 140 km wider than the IW mode. Clearly visible in both figures are the five and three subswaths of the EW and IW mode, respectively, as the noise increases towards the edges as a consequence of the antenna pattern. In reality the subswaths overlap partly, so that the noise can be reduced by approximately $\sqrt{2}$ at the

https://doi.org/10.5194/tc-2020-245
Preprint. Discussion started: 30 October 2020

edges. For the first subswath of the EW mode the antenna beamwidth should be widened to limit the increase in noise near the edges.

The wider swath of the EW mode comes at the cost of resolution, which decreases the number of independent looks for averaging. The reduced number leads to a worse precision of the velocity measurements, which is more-or-less a factor of $\sqrt{8}$ (see previous section). This greatly reduces the ability to detect individual flows and discontinuities in the velocity field. The change of Sentinel-1D to the IW mode, which we opt for, comes at the cost of the number of passes (figure 6). Above 74° latitude, the maximum number of passes in EW mode over any point is above twelve times per repeat-orbit, or once per day for a single Sentinel-1 satellite. By switching to the IW mode, this number will drop to about once per 1.5 day at the same latitude. Above 80° the number of once per day is still reached. For the sea ice surrounding Antarctica, which is located at lower latitudes, the sampling rate will be typically around once per two days. Note that several other satellites will be operated in C- and L-band in 2028, such as Sentinel-C, the RADARSAT constellation and L-ROSE, which ensure a sampling rate of better than once per day for speckle tracking.

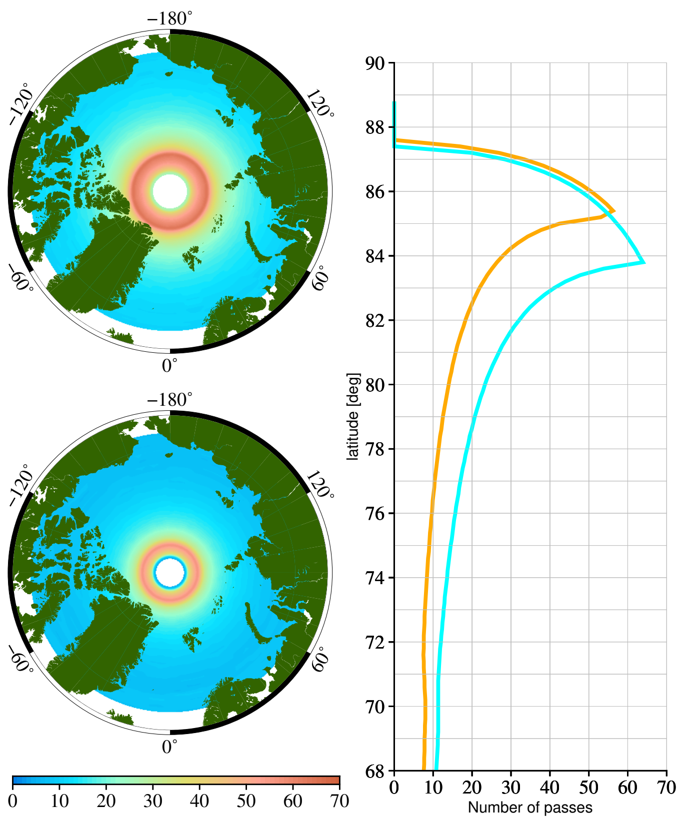

Figure 6. Maximum number of acquisitions within the 12-day repeat period for the EW mode (top, light-blue) and the IW mode (bottom, orange) as a function of latitude and geographically.

https://doi.org/10.5194/tc-2020-245
Preprint. Discussion started: 30 October 2020

The great gain of having Harmony in stereo mode over sea ice is the ability to estimate instantaneous velocities, rather than only daily integrated values (figure 7). As shown in the figure, the velocity fields tend to change on sub-daily timescales, which leads to aliasing when only speckle tracking is applied. The differences between daily and instantaneous observations becomes even more apparent if the deformation is computed from the velocity fields. As a result the total energy transfer is underestimated in current daily-integrated velocities as also discussed in other studies (Dierking et al., 2017; Dammann et al., 2019). The differences between daily integrated and instantaneous velocity are linked to short-term events, like the opening and closing of leads, floe collision and break-up. Harmony data allows to compute enhanced statistics on these type of events, which is beneficial for parametrization and calibration of sea-ice models The addition of instantaneous velocities at two epochs will also enhance the interpretation of daily integrated velocities, as the motion does not have to be linear, which is assumption in speckle tracking (Kwok et al., 1990).

Finally, in stereo formation, as long as the surface NRCS is sufficient (higher than ~ -25 dB), Harmony will be able to provide two-dimensional velocity estimates over any surface. This implies that velocity estimates can be obtained in the marginal ice zone over small and highly dynamic floes, where traditional methods as speckle tracking have problems. In occasions when the water surface is exposed to strong winds, it is even possible to determine the velocity in leads, as already demonstrated with Tandem-X (Dammann et al., 2019). The separation of ocean surface current and sea-ice drift gives the opportunity to estimate drag parameters if accurate wind estimates are available as well.

3.3 Sea-ice drift and deformation

Figure 8 shows the estimated velocity fields from Harmony at 2 km $\times$ 2 km multilooking based on the neXtSIM model input. The figure demonstrates the result of the inferior along-track accuracy as discussed in section 3.1. Furthermore, the effect of the antenna pattern is visible, because the noise increases near the edges of the subswaths. Without filtering, the velocity fields are difficult to interpret and to process.

An adaptive Wiener filter is applied to reduce the noise, while it keeps the edges intact. Low-pass filters are less suitable, because edges require directional high-frequency harmonics, which would be suppressed. With a Wiener filter some higher frequencies are retained, such that the resolution effectively varies with direction. Application of the Wiener filter reduces the root-mean-square of differences between the neXtSIM velocity fields and the filtered velocities from 6.8 cm s^{-1} to 1.0 cm s^{-1} and from 2.4 cm s^{-1} to 0.4 cm s^{-1} for the azimuth and ground-range directions, respectively. The histograms in figure 8 show that Harmony is able to accurately capture the distribution of the velocities in both directions, as the differences with input fields are minimal.

We also derive the structure and deformation patterns of the sea ice, which would not be possible with speckle tracking. Using edge detection methods for the velocity fields, we can identify individual flows (third and sixth panel of figure 8) and compute the shear and divergence at the edges of the floes (figure 9). This allows to extract statistics on the structure of sea ice, for example the floe size, even if there is no lead in between the floes. The estimated divergence at the edges indicates locations where leads open and close, and also identify locations where ridges might form as a consequence of collisions. Shear

https://doi.org/10.5194/tc-2020-245
Preprint. Discussion started: 30 October 2020

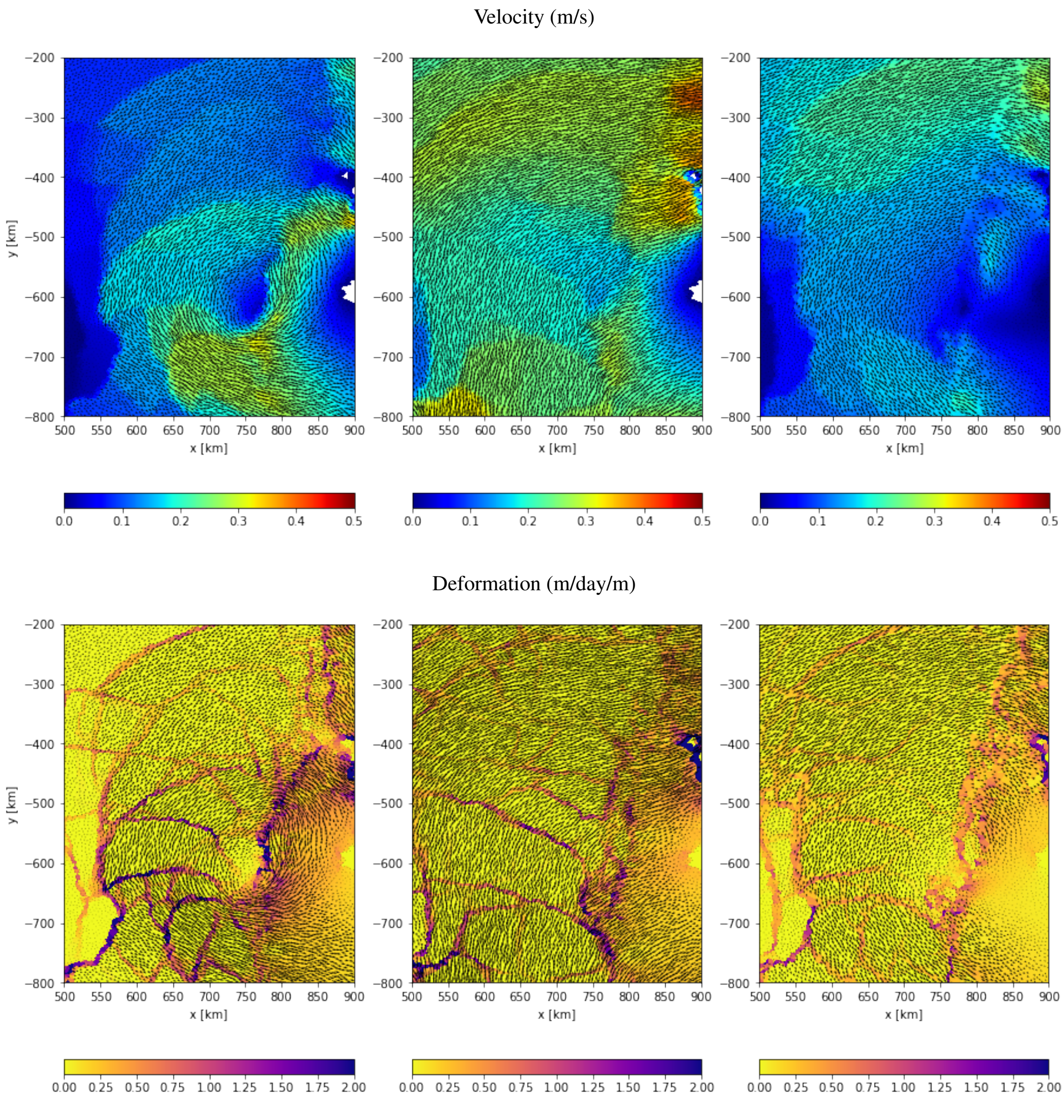

Figure 7. Instantaneous sea-ice velocities at two epochs separated by a day (top-left and top-middle) and daily integrated velocities (top-right) as estimated from the neXtSIM sea-ice model. In the bottom the associated deformation.

estimates are useful to determine sea-ice stress estimates and both shear and divergence are a source of information for local wind and ocean drag on sea ice. Statistics on these processes cannot be obtained with any operation mission currently flown.

The top histogram in figure 9 shows that the estimated shear at the boundaries follows a Rayleigh distribution. The absence of small shear is contributed to the limit of what we are able to extract with Harmony. Harmony, in combination with the proposed method is only able to reveal shear larger than 0.5 cm s^{-1} km^{-1}, which might be enhanced by other more suitable signal processing strategies once it flies. Secondly, the shear is inevitably a bit underestimated due to the applied filter. Less filtering decreases the underestimation, but introduces more noise in velocity estimates, which also has a consequence for the

https://doi.org/10.5194/tc-2020-245
Preprint. Discussion started: 30 October 2020

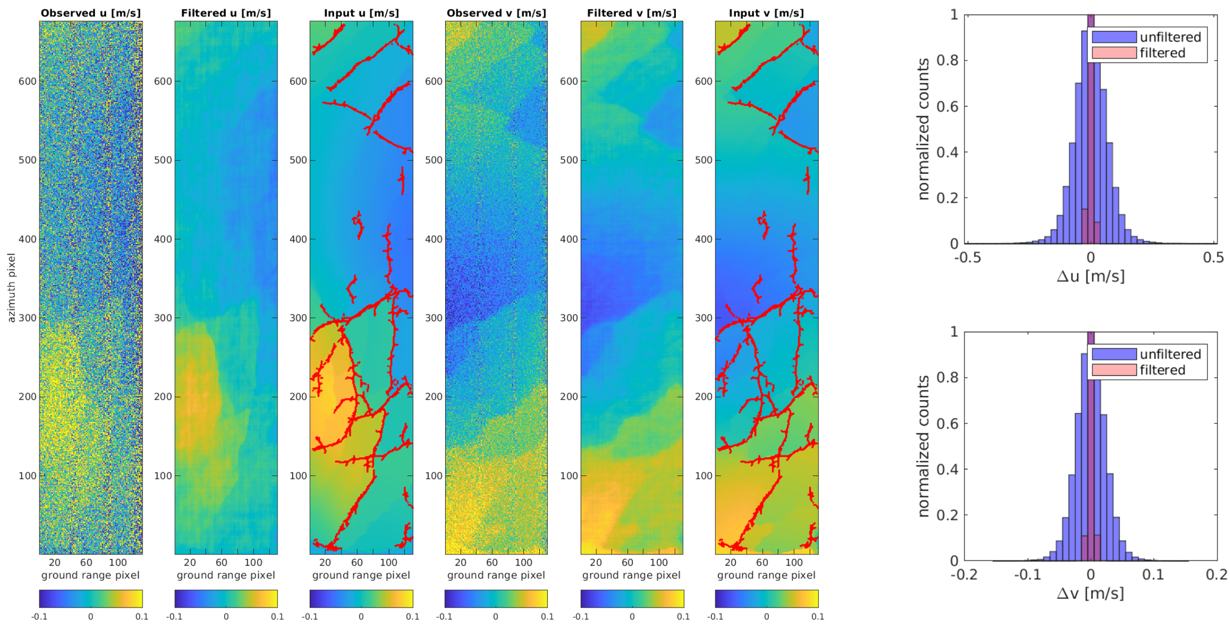

Figure 8. Azimuth and ground-range direction velocities retrieved by Harmony before and after application of the adaptive Wiener filter. The input data is also given with in red the detected discontinuities. The histograms on the right show the differences between the input and retrieved velocities before and after Wiener filtering.

distribution. Following the equation for the divergence in sect 2.4, a higher noise in the gradients causes it also to be less likely for small divergence to occur. It is therefore recommended that tailored filters should be applied, depending on the applications and whether divergence or shear is considered, which can for example be done by scaling the noise parameter in the adaptive Wiener filter (sect 2.4).

3.4 Wave spectra

Swell waves propagating in the azimuth direction modulate the amplitudes through velocity bunching, which is an artefact of focusing SAR images over non-stationary targets with harmonic behavior (Hasselmann and Hasselmann, 1991). As scatterers from different parts of the swell wave have different range velocities, they introduce small Doppler effects that cause clustering of scatterers in azimuth. This pattern is predictable and is therefore already used to infer swell properties based on intensity spectra from Sentinel-1 data. Velocity bunching does not occur when swell waves propagate in the ground-range direction and are therefore not captured with a monostatic SAR system alone. For a bi-static system the ground-range direction is approxi-

https://doi.org/10.5194/tc-2020-245
Preprint. Discussion started: 30 October 2020

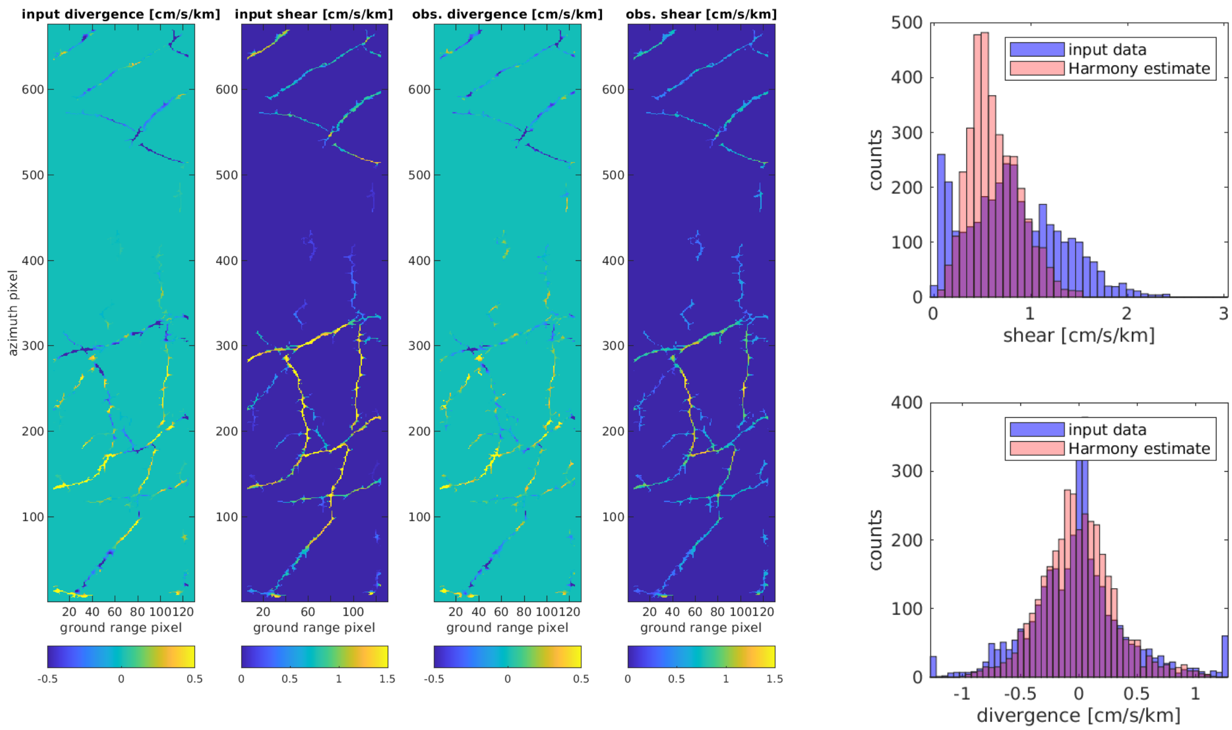

Figure 9. Estimated divergence and shear at the discontinuities from the input data and from the Wiener filtered data. The histograms show the distributions of the estimated divergence and shear over the same swath.

mately aligned with the midpoint between the transmitter and receiver, referred to as the equivalent monostatic system. Since the proposed Harmony mission uses two receivers and Sentinel-1D itself acts as one, in Stereo mode there are three lines-of-sight, each separated by approximately 16° (half the bi-static angle). This allows to infer swell properties in any direction as the gap is typically smaller than this. When orbiting in the XTI formation, one line-of-sight is lost, such that we lose sensitivity to swell in the directions between the effective ground-range directions (-16° to 0°) of Harmony XTI and Sentinel-1D. Fortunately, the XTI phase difference also allows us to directly infer elevations and from that wave spectra. The interferometric XTI phase difference only relies on the position of the receivers. An angle of zero in our simulations would therefore be equivalent to waves propagating in the ground-range direction of the two Harmony satellites, or approximately -32°. Effectively, the XTI formation has therefore three lines-of-sight: Sentinel-1D, Harmony and the XTI formation. A combination between intensity and elevation spectra would therefore cross-calibrate and constrain the swell properties in both directions. Besides that, phase-

https://doi.org/10.5194/tc-2020-245
Preprint. Discussion started: 30 October 2020

difference spectra have the advantage that they are less sensitive to contamination than the intensity spectrum by for example ice ridges (Ardhuin et al., 2017).

Figure 10 shows the elevations, the intensity and normalized elevation spectra computed from OceanSAR simulations of an ice surface that is exposed to swell waves in four directions. The peaks in the intensity spectra are expected at $(\cos\phi_w, \sin\phi_w)$ with ϕ_w the direction of the wave propagation. Note again that $\phi_w = 0$ is the effective range direction of the bi-static system, which is in case or Harmony about $-16°$ from the cross-track direction. This is indeed true for the intensity spectra, which furthermore show the virtual absence of sensitivity to swell in the ground-range direction. Interpretation of the spectra is not straightforward as velocity bunching enhances the peaks in the intensity images, which leads to secondary peaks in the observed spectra. Additionally, the velocity variance of the surface causes signals at high wave numbers to dampen (Krogstad et al., 1994), which is of primary importance near the sea-ice edge where wind waves have not been fully dampened yet. Spectral transforms, taking into account both effects are required to infer wave amplitude or energy (Ardhuin et al., 2017; Hasselmann and Hasselmann, 1991; Krogstad et al., 1994). At the moment of writing, bi-static transforms to convert ocean wave spectra into intensity spectra are being developed, which will be addressed in a separate paper.

The elevation spectra in figure 10 show the sensitivity to waves propagating in the receiver range, which is directed about -32°, from the cross-track direction. After normalization, the amplitude of the wave propagating in the receiver range direction ($\phi_w = 0°$) is close to the expected value of 2 meter. This, however changes whenever ϕ_w is different, which is the consequence of the SAR image distortions as a consequence of a moving surface that change the retrieved elevation pattern. At larger azimuth angles, the amplitude reduces further, such that waves propagating in the flight direction are almost not detectable. In practice, this means that the inferred XTI height cannot directly be used to estimate wave height, but spectral transforms or geophysical model functions are required. The bi-static transforms to estimate wave height from phase information are yet to be developed.

Swell is detectable using SAR intensity spectra if the wave height is a few decimeters (Ardhuin et al., 2017), depending on the wave direction and the distance from the ice edge. The Stereo configuration of Harmony satellites provides better constrains of the wave spectra in case waves are propagating near the range direction, but it also allows to cross-calibrate the spectra against each other. In XTI formation, once spectral transforms have been developed, two quasi-independent methods (height and intensity spectra) allow for the recovery of swell spectra in all directions plus again a cross-calibration of the swell-wave spectra derived from those methods. In both formations, Harmony data allows for a full two-dimensional ray-tracing of swell waves from a single pass up to their dissipation until several decimeters height. This enables us to better constrain dissipation parameters when waves propagate under sea ice.

4 Conclusions

We presented the observation principle, several processing methods and the simulated performance of Harmony for sea ice. Harmony's formation with Sentinel-1D is reconfigurable and will operate in a stereo formation and an cross-track interferometry (XTI) formation. There are two main benefits of the bi-static stereo mode operation with respect to currently-operated

https://doi.org/10.5194/tc-2020-245
Preprint. Discussion started: 30 October 2020

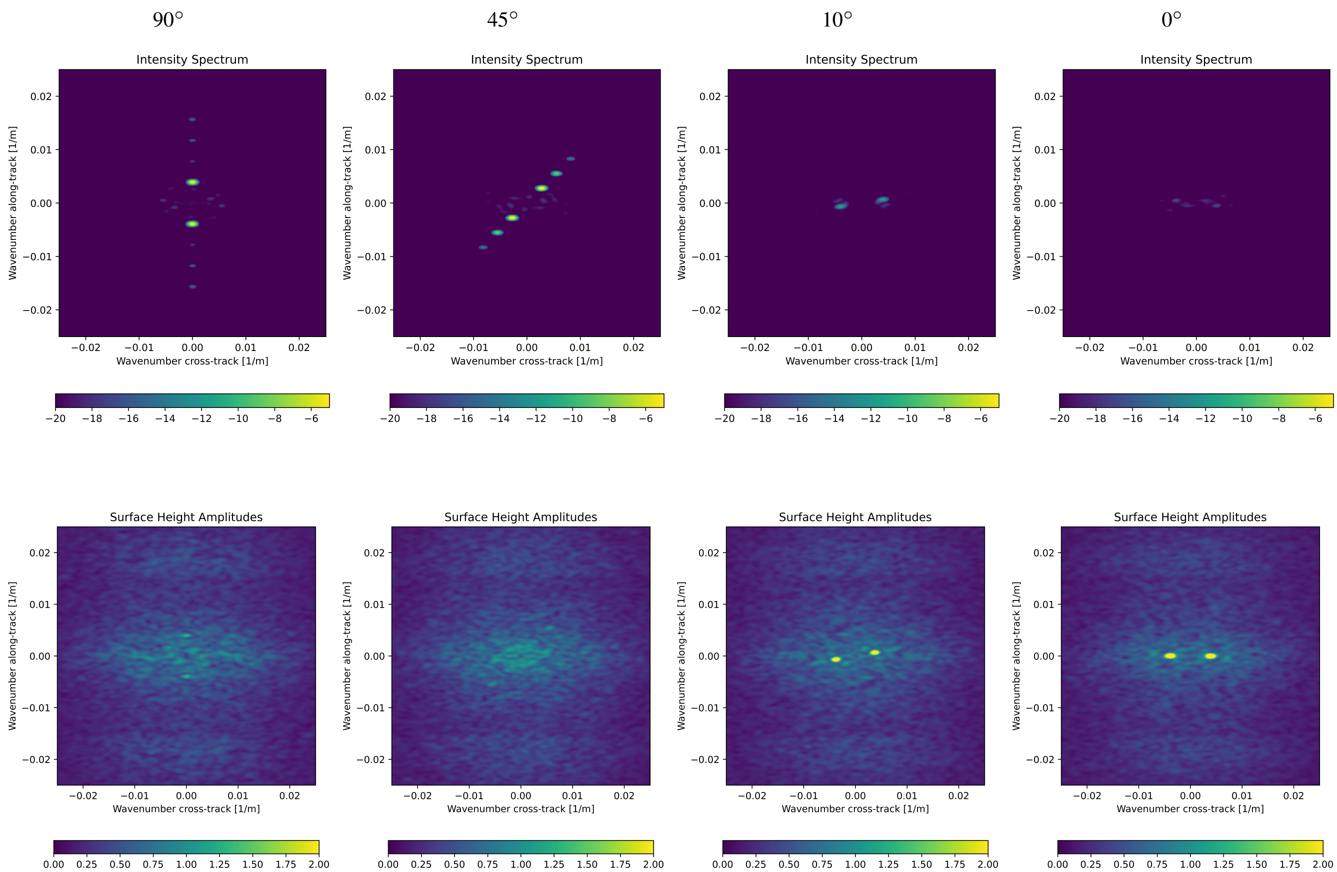

Figure 10. Observed intensity (log-scale) and elevation amplitude spectra (m) for 256-meter long, 2-meter high swell waves propagating in different directions. The 90°-direction corresponds to waves propagating in the azimuth direction.

monostatic missions, which are the abilities to vectorize the sea-ice drift estimates and to obtain instantaneous observations. The XTI mode has the benefit of instantly retrieving phase difference, so that decorrelation due to fast motion is minimal.

Harmony's stereo mode data will allow for the estimation of two-dimensional sea-ice drift fields and infer shear and divergence at floe boundaries. Both are required for the calibration of models and to determine local sea-ice properties. Due to limited the geometry of the constellation has the estimated cross-track velocity a lower uncertainty than the along-track velocity. Advanced post-processing strategies, like filtering and edge detection, are required to get the maximum out of the data. The performance is strongly enhanced by switching Sentinel-1D operations from the EW to the IW mode over sea ice. As the choice to operate Sentinel-1 in EW mode was driven by sea-ice community, we recommend a change of modes over the sea-ice-covered regions.

Harmony also enable the estimation of two-dimensional swell-wave spectra and wave dissipation constants. It will not only enhance the understanding of wave propagation, but also improve the understanding of energy transfer to the ice, which could

https://doi.org/10.5194/tc-2020-245
Preprint. Discussion started: 30 October 2020

The Cryosphere Discussions

lead to events like breaking. In the stereo mode, Harmony will benefit from multiple lines-of-sight to remove the blind spot (i.e. swell propagating in the range direction) present in monostatic systems, and can use three observations from different angles to cross-calibrate the geophysical transfer model. In XTI mode, Harmony benefits from the instantaneous elevation retrieval, which is most sensitive to swell propagating in the receiver line-of-sight, while having two lines-of-sight for traditional velocity-bunching based spectra retrievals.

Author contributions. M.K., A.T., Y.L. and P.L. performed the computations. A.K. performed the neXtSIM sea-ice model runs. M.K. and P.L. wrote the manuscript. All authors contributed to the discussion and reviewed the manuscript.

Competing interests. Declarations of interest: none.

Acknowledgements. The authors would like to thank Alexander Komarov for his support with the implementation of the sea-ice backscatter model. This activity was funded by the Dutch Space Office (NSO) in support of the Harmony Phase-0 studies (ref. NFBINS1903).

The Cryosphere Discussions
Open Access EGU

References

Ardhuin, F., Stopa, J., Chapron, B., Collard, F., Smith, M., Thomson, J., Doble, M., Blomquist, B., Persson, O., Collins, C. O., and Wadhams, P.: Measuring ocean waves in sea ice using SAR imagery: A quasi-deterministic approach evaluated with Sentinel-1 and in situ data, Remote Sensing of Environment, 189, 211–222, https://doi.org/10.1016/j.rse.2016.11.024, https://linkinghub.elsevier.com/retrieve/pii/S0034425716304710, 2017.

Armitage, T. W. K. and Ridout, A. L.: Arctic sea ice freeboard from AltiKa and comparison with CryoSat-2 and Operation IceBridge, Geophysical Research Letters, 42, 6724–6731, https://doi.org/10.1002/2015GL064823, https://onlinelibrary.wiley.com/doi/abs/10.1002/2015GL064823, 2015.

Dammann, D. O., Eriksson, L. E. B., Mahoney, A. R., Eicken, H., and Meyer, F. J.: Mapping pan-Arctic landfast sea ice stability using Sentinel-1 interferometry, The Cryosphere, 13, 557–577, https://doi.org/10.5194/tc-13-557-2019, https://www.the-cryosphere.net/13/557/2019/, 2019.

Dierking, W.: Mapping of Different Sea Ice Regimes Using Images From Sentinel-1 and ALOS Synthetic Aperture Radar, IEEE Transactions on Geoscience and Remote Sensing, 48, 1045–1058, https://doi.org/10.1109/TGRS.2009.2031806, http://ieeexplore.ieee.org/document/5308452/, 2010.

Dierking, W., Lang, O., and Busche, T.: Sea ice local surface topography from single-pass satellite InSAR measurements: a feasibility study, The Cryosphere, 11, 1967–1985, https://doi.org/10.5194/tc-11-1967-2017, https://www.the-cryosphere.net/11/1967/2017/, 2017.

Duque, S., Lopez-Dekker, P., Merlano, J. C., and Mallorqui, J. J.: Bistatic SAR along track interferometry with multiple fixed receivers, in: 2010 IEEE International Geoscience and Remote Sensing Symposium, pp. 4099–4102, IEEE, Honolulu, HI, USA, https://doi.org/10.1109/IGARSS.2010.5652057, http://ieeexplore.ieee.org/document/5652057/, 2010.

Filhol, S. and Sturm, M.: Snow bedforms: A review, new data, and a formation model, Journal of Geophysical Research: Earth Surface, 120, 1645–1669, 2015.

Haller, M., Brümmer, B., and Müller, G.: Atmosphere–ice forcing in the transpolar drift stream: results from the DAMOCLES ice-buoy campaigns 2007–2009, The Cryosphere, 8, 275–288, https://doi.org/10.5194/tc-8-275-2014, https://www.the-cryosphere.net/8/275/2014/, 2014.

Hasselmann, K. and Hasselmann, S.: On the nonlinear mapping of an ocean wave spectrum into a synthetic aperture radar image spectrum and its inversion, Journal of Geophysical Research: Oceans, 96, 10 713–10 729, https://doi.org/10.1029/91JC00302, https://agupubs.onlinelibrary.wiley.com/doi/abs/10.1029/91JC00302, 1991.

Kleinherenbrink, M., Lopez-Dekker, P., Newman, T., Johnsen, H., and Chapron, B.: Ocean surface currents and sea-ice velocity estimation strategies and preliminary performances for the Harmony mission., ARSI conference, https://www.researchgate.net/publication/341371509_Ocean_surface_currents_and_sea-ice_velocity_estimation_strategies_and_preliminary_performances_for_the_Harmony_mission, 2019.

Komarov, A. S., Shafai, L., and Barber, D. G.: ELECTROMAGNETIC WAVE SCATTERING FROM ROUGH BOUNDARIES INTERFACING INHOMOGENEOUS MEDIA AND APPLICATION TO SNOW-COVERED SEA ICE, Progress In Electromagnetics Research, 144, 201–219, https://doi.org/10.2528/PIER13111209, http://www.jpier.org/PIER/pier.php?paper=13111209, 2014.

Komarov, A. S., Isleifson, D., Barber, D. G., and Shafai, L.: Modeling and Measurement of C-Band Radar Backscatter From Snow-Covered First-Year Sea Ice, IEEE Transactions on Geoscience and Remote Sensing, 53, 4063–4078, https://doi.org/10.1109/TGRS.2015.2390192, http://ieeexplore.ieee.org/document/7047848/, 2015.

https://doi.org/10.5194/tc-2020-245
Preprint. Discussion started: 30 October 2020

Krogstad, H. E., Samset, O., and Vachon, P. W.: Generalizations of the non-linear ocean-SAR transform and a simplified SAR inversion algorithm, Atmosphere-Ocean, 32, 61–82, https://doi.org/10.1080/07055900.1994.9649490, https://doi.org/10.1080/07055900.1994.9649490, 1994.

Krupnik, I., Aporta, C., Gearheard, S., Laidler, G.J., and L., K. H.: SIKU: Knowing Our Ice, Springer, 2010.

Kwok, R. and Cunningham, G. F.: Backscatter characteristics of the winter ice cover in the Beaufort Sea, Journal of Geophysical Research, 99, 7787, https://doi.org/10.1029/94JC00169, http://doi.wiley.com/10.1029/94JC00169, 1994.

Kwok, R., Curlander, J., McConnell, R., and Pang, S.: An ice-motion tracking system at the Alaska SAR facility, IEEE Journal of Oceanic Engineering, 15, 44–54, https://doi.org/10.1109/48.46835, http://ieeexplore.ieee.org/document/46835/, 1990.

Landy, J. C., Tsamados, M., and Scharien, R. K.: A Facet-Based Numerical Model for Simulating SAR Altimeter Echoes From Heterogeneous Sea Ice Surfaces, IEEE Transactions on Geoscience and Remote Sensing, 57, 4164–4180, https://doi.org/10.1109/TGRS.2018.2889763, https://ieeexplore.ieee.org/document/8625441/, 2019.

Lindsay, R. and Schweiger, A.: Arctic sea ice thickness loss determined using subsurface, aircraft, and satellite observations, The Cryosphere, 9, 269–283, https://doi.org/10.5194/tc-9-269-2015, https://www.the-cryosphere.net/9/269/2015/, 2015.

Long, D. G.: Polar Applications of Spaceborne Scatterometers, IEEE Journal of Selected Topics in Applied Earth Observations and Remote Sensing, 10, 2307–2320, https://doi.org/10.1109/JSTARS.2016.2629418, http://ieeexplore.ieee.org/document/7781629/, 2017.

López-Dekker, P., Rott, H., Prats-Iraola, P., Chapron, B., Scipal, K., and Witte, E. D.: Harmony: an Earth Explorer 10 Mission Candidate to Observe Land, Ice, and Ocean Surface Dynamics, in: IGARSS 2019 - 2019 IEEE International Geoscience and Remote Sensing Symposium, pp. 8381–8384, https://doi.org/10.1109/IGARSS.2019.8897983, 2019.

Madsen, S.: Estimating the Doppler centroid of SAR data, IEEE Transactions on Aerospace and Electronic Systems, 25, 134–140, https://doi.org/10.1109/7.18675, http://ieeexplore.ieee.org/document/18675/, 1989.

Notz, D., Dörr, J., Bailey, D. A., Blockley, E., Bushuk, M., Debernard, J. B., Dekker, E., DeRepentigny, P., Docquier, D., Fučkar, N. S., Fyfe, J. C., Jahn, A., Holland, M., Hunke, E., Iovino, D., Khosravi, N., Massonnet, F., Madec, G., O'Farrell, S., Petty, A., Rana, A., Roach, L., Rosenblum, E., Rousset, C., Semmler, T., Stroeve, J., Tremblay, B., Toyoda, T., Tsujino, H., and Vancoppenolle, M.: Arctic Sea Ice in CMIP6, Geophysical Research Letters, https://doi.org/10.1029/2019GL086749, https://onlinelibrary.wiley.com/doi/abs/10.1029/2019GL086749, 2020.

Parkinson, C. L.: A 40-y record reveals gradual Antarctic sea ice increases followed by decreases at rates far exceeding the rates seen in the Arctic, Proceedings of the National Academy of Sciences, 116, 14 414–14 423, https://doi.org/10.1073/pnas.1906556116, http://www.pnas.org/lookup/doi/10.1073/pnas.1906556116, 2019.

Price, D., Soltanzadeh, I., Rack, W., and Dale, E.: Snow-driven uncertainty in CryoSat-2-derived Antarctic sea ice thickness – insights from McMurdo Sound, The Cryosphere, 13, 1409–1422, https://doi.org/10.5194/tc-13-1409-2019, https://www.the-cryosphere.net/13/1409/2019/, 2019.

Rampal, P., Bouillon, S., Ólason, E., and Morlighem, M.: neXtSIM: a new Lagrangian sea ice model, The Cryosphere, 10, 1055–1073, https://doi.org/10.5194/tc-10-1055-2016, https://www.the-cryosphere.net/10/1055/2016/, 2016.

Rampal, P., Dansereau, V., Olason, E., Bouillon, S., Williams, T., Korosov, A., and Samaké, A.: On the multi-fractal scaling properties of sea ice deformation, The Cryosphere, 13, 2457–2474, https://doi.org/10.5194/tc-13-2457-2019, https://www.the-cryosphere.net/13/2457/2019/, 2019.

Ricker, R., Hendricks, S., Helm, V., Skourup, H., and Davidson, M.: Sensitivity of CryoSat-2 Arctic sea-ice freeboard and thickness on radar-waveform interpretation, The Cryosphere, 8, 1607–1622, https://doi.org/10.5194/tc-8-1607-2014, https://www.the-cryosphere.net/8/1607/2014/, 2014.

Ricker, R., Hendricks, S., Girard-Ardhuin, F., Kaleschke, L., Lique, C., Tian-Kunze, X., Nicolaus, M., and Krumpen, T.: Satellite-observed drop of Arctic sea ice growth in winter 2015-2016: REDUCED ICE GROWTH IN 2015-2016, Geophysical Research Letters, 44, 3236–3245, https://doi.org/10.1002/2016GL072244, http://doi.wiley.com/10.1002/2016GL072244, 2017.

Rosen, P., Hensley, S., Joughin, I., Li, F., Madsen, S., Rodriguez, E., and Goldstein, R.: Synthetic aperture radar interferometry, Proceedings of the IEEE, 88, 333–382, https://doi.org/10.1109/5.838084, http://ieeexplore.ieee.org/document/838084/, 2000.

Scheiber, R., De Zan, F., Prats, P., Sant'Anna Araujo, L., Kunemund, M., and Marotti, L.: Interferometric sea ice mapping with TanDEM-X: First experiments, in: 2011 IEEE International Geoscience and Remote Sensing Symposium, pp. 3594–3597, IEEE, Vancouver, BC, Canada, https://doi.org/10.1109/IGARSS.2011.6050001, http://ieeexplore.ieee.org/document/6050001/, 2011.

Scheuchl, B., Cumming, I., and Hajnsek, I.: Classification of fully polarimetric single-and dual-frequency SAR data of sea ice using the Wishart statistics, Canadian Journal of Remote Sensing, 31, 61–72, 2005.

Shokr, M.: Compilation of a radar backscatter database of sea ice types and open water using operational analysis of heterogeneous ice regimes, Canadian Journal of Remote Sensing, 35, 369–384, 2009.

Squire, V. A.: A fresh look at how ocean waves and sea ice interact, Philosophical Transactions of the Royal Society A: Mathematical, Physical and Engineering Sciences, 376, 20170 342, https://doi.org/10.1098/rsta.2017.0342, https://royalsocietypublishing.org/doi/10.1098/rsta.2017.0342, 2018.

Stopa, J. E., Ardhuin, F., Thomson, J., Smith, M. M., Kohout, A., Doble, M., and Wadhams, P.: Wave Attenuation Through an Arctic Marginal Ice Zone on 12 October 2015: 1. Measurement of Wave Spectra and Ice Features From Sentinel 1A, Journal of Geophysical Research: Oceans, 123, 3619–3634, https://doi.org/10.1029/2018JC013791, http://doi.wiley.com/10.1029/2018JC013791, 2018.

Stroeve, J. and Notz, D.: Changing state of Arctic sea ice across all seasons, Environmental Research Letters, 13, 103 001, https://doi.org/10.1088/1748-9326/aade56, https://iopscience.iop.org/article/10.1088/1748-9326/aade56, 2018.

Sumata, H., Lavergne, T., Girard-Ardhuin, F., Kimura, N., Tschudi, M. A., Kauker, F., Karcher, M., and Gerdes, R.: An intercomparison of Arctic ice drift products to deduce uncertainty estimates, Journal of Geophysical Research: Oceans, 119, 4887–4921, https://doi.org/10.1002/2013JC009724, http://doi.wiley.com/10.1002/2013JC009724, 2014.

Ulaby, F. and Long, D.: Microwave radar and radiometric remote sensing, Artech House, 2015.